Modeling the nominal flexural strength of w-shape beams using a new inelastic model

Barry T. Rosson[1], Matthew F. Fadden[2]

Abstract

An inelastic material model was developed and validated for use as normalized tangent modulus expressions in *MASTAN2* for major-axis and minor-axis beam bending conditions. Limit load analyses were conducted using the new material model with 14-DOF beam elements in *MASTAN2* and were compared with published finite element results. The validation study over a range of different beam cross-section and loading conditions revealed close agreement with the published results. Discussion and recommendations are provided regarding the material model and its use when following the design provisions of Appendix 1.3 in the AISC *Specification for Structural Steel Buildings*.

1. Introduction

Appendix 1 in AISC 360-16 (2016) provides the designer with the option to use advanced methods of structural analysis to directly model localized yielding and its effects on system behavior. The analysis requirements stipulate that the second-order inelastic analysis must account for geometric imperfections and the influence of residual stresses and partial yielding effects. Recent research has focused on developing design procedures and equations to account for the reduction in stiffness due to partial yielding effects (Kucukler *et al*. 2104, Rosson and Ziemian 2019, Subramanian and White 2017a and 2017b, Tankova *et al*. 2017). The primary goal of this research is to provide designers with an accurate and efficient material model for a 14-DOF beam element when using the direct modeling provisions in Appendix 1 to determine the lateral torsional buckling (LTB) capacity of rolled I-section beams.

2. Stiffness Reduction Model

The proposed stiffness reduction (τ) model that accounts for partial yielding of the beam's cross-section due to uniaxial or biaxial bending moments is given in Fig. 1. The triangular plateau at the top of the model represents the moment conditions for which yielding does not occur ($\tau = 1$). The dashed red curve represents the stiffness reduction due to moments beyond the yield plateau and is assumed to vary as an exponential function between 1 and 0. The blue curve at the bottom represents the biaxial moment conditions at which $\tau = 0$ and is assumed to vary as a second-order

---

[1] Professor, Florida Atlantic University, <rosson@fau.edu>
[2] Senior Associate, Wiss, Janney, Elstner Associates, Inc., <mfadden@wje.com>

polynomial defined by the three coordinates $(1,0,0)$, $(m_z^*, m_y^*, 0)$ and $(0,1,0)$. The model variables are a function of the W-shape's cross-section dimensions, the residual stress ratio c_r, and the exponents n_z and n_y for the curves along the $\boldsymbol{m_z}$ and $\boldsymbol{m_y}$ axes, respectively.
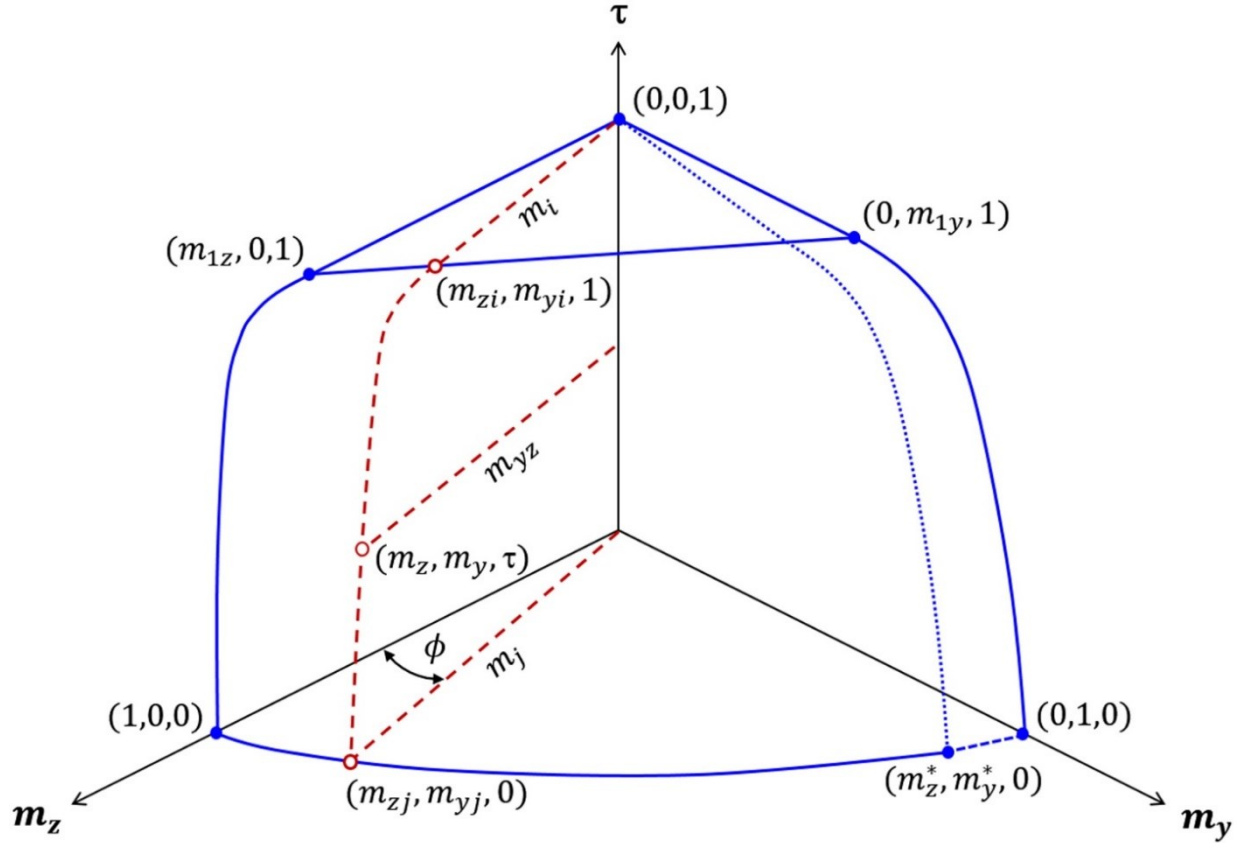

Figure 1: Stiffness reduction model with variable definitions for major-axis and minor-axis bending

The major-axis moment M_z and minor-axis moment M_y are normalized using the respective plastic moment capacities as $m_z = M_z/M_{pz}$ and $m_y = M_y/M_{py}$. For a given W-shape, and assuming an ECCS residual stress pattern (1984), the maximum moment for which $\tau = 1$ is maintained for uniaxial major-axis bending is

$$m_{1z} = \frac{S_z}{Z_z}(1 - c_r) \tag{1}$$

where S_z = major-axis elastic section modulus, Z_z = major-axis plastic section modulus and c_r = residual stress ratio (σ_r/σ_y). The similar equation for uniaxial minor-axis bending is

$$m_{1y} = \frac{S_y}{Z_y}(1 - c_r) \tag{2}$$

where S_y = minor-axis elastic section modulus and Z_y = minor-axis plastic section modulus.

2

The m_{zi} and m_{yi} coordinates in Fig. 1 are found assuming a linear relationship between m_{1z} and m_{1y}.

$$m_{zi} = \frac{m_{1y}}{\dfrac{m_y}{m_z} + \dfrac{m_{1y}}{m_{1z}}} \tag{3}$$

$$m_{yi} = \frac{m_y}{m_z} m_{zi} \tag{4}$$

Using the m_{zi} and m_{yi} values, the m_i scalar magnitude in Fig. 1 is

$$m_i = \sqrt{m_{zi}^2 + m_{yi}^2} \tag{5}$$

The m_z^* and m_y^* coordinates in Fig. 1 are determined from the dimensions of the W-shape and correspond to the moments for the plastic neutral axis to be in the position as given in Fig. 2. This coordinate is unique to every W-shape and helps to accurately define the $\tau = 0$ curve in Fig. 1.
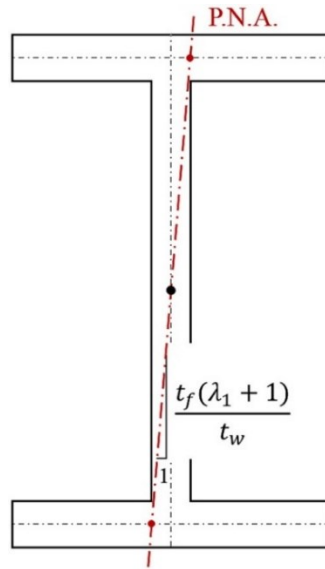

Figure 2: Plastic neutral axis at m_z^* and m_y^*

The closed-form equations for m_z^* and m_y^* are

$$m_z^* = \frac{\lambda\lambda_1 + 6\lambda + 5\lambda_o}{\lambda\lambda_1 + 4\lambda_1 + 4} \tag{6}$$

$$m_y^* = \frac{1}{2 + \lambda\lambda_0}\left(2 - \frac{[(4(\lambda_1 + 1) + \lambda\lambda_1)m_z^* - \lambda_o(\lambda_1 + 1)^2]^2}{8(\lambda_1 + 1)^2}\right) \tag{7}$$

where $\lambda = A_w/A_f$, $\lambda_0 = t_w/b_f$ and $\lambda_1 = d_w/t_f$ (Rosson 2016).

By way of example, the red curve in Fig. 3 is the biaxial moment condition at $\tau = 0$ for a W14x53 based on a detailed fiber element analysis. This curve is approximated using a second-order polynomial as given by the blue curve in Fig. 3. A linear approximation as given by the dashed blue line in Fig. 3 is used between (m_z^*, m_y^*) and $(0, 1)$ to ensure that $m_{yj} \leq 1$.

In the assumed quadratic region, the m_{zj} and m_{yj} coordinate values are found using

$$m_{yj} = C_1 m_{zj}^2 + C_2 m_{zj} + 1 \qquad (8)$$

where the constants C_1 and C_2 are determined using the m_z^* and m_y^* values from Eqs. 6 and 7.

$$C_1 = \frac{1 - m_z^* - m_y^*}{m_z^* - m_z^{*2}} \qquad (9)$$

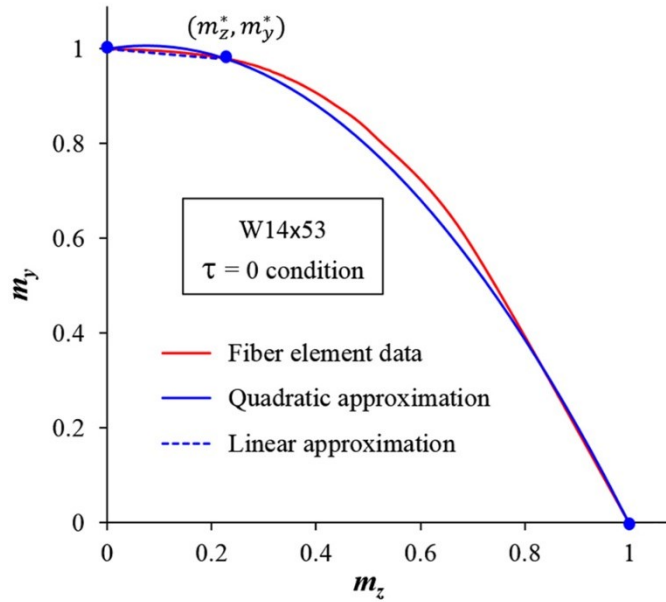$$C_2 = \frac{m_z^{*2} - m_y^* - 1}{m_z^* - m_z^{*2}} \qquad (10)$$

Figure 3: Actual and approximate biaxial moments m_{zj} and m_{yj} at $\tau = 0$

The m_{zj} coordinate along the blue curve is defined by

$$\text{when } \frac{m_y}{m_z} \leq \frac{m_y^*}{m_z^*} \qquad m_{zj} = \frac{\left(\frac{m_y}{m_z} - C_2\right) - \sqrt{\left(\frac{m_y}{m_z} - C_2\right)^2 - 4C_1}}{2C_1} \qquad (11)$$

and the m_{zj} coordinate along the dashed blue line is defined by

$$when \ \frac{m_y}{m_z} > \frac{m_y^*}{m_z^*} \qquad\qquad m_{zj} = \frac{1}{\frac{m_y}{m_z} - \left(\frac{m_y^* - 1}{m_z^*}\right)} \qquad\qquad (12)$$

Using the m_{zj} coordinate from either Eq. 11 or 12, the m_{yj} coordinate is found using

$$m_{yj} = \frac{m_y}{m_z} m_{zj} \qquad\qquad (13)$$

The m_j scalar magnitude in Fig. 1 is found using the m_{zj} and m_{yj} values.

$$m_j = \sqrt{m_{zj}^2 + m_{yj}^2} \qquad\qquad (14)$$

The m_{yz} scalar magnitude in Fig. 1 is found in the same way using the m_z and m_y values.

$$m_{yz} = \sqrt{m_z^2 + m_y^2} \qquad\qquad (15)$$

Finally, for a given m_z and m_y moment condition, the stiffness reduction can be determined using Eqs. 5, 14 and 15.

$$when \ m_{yz} \leq m_i \qquad\qquad \tau = 1 \qquad\qquad (16)$$

$$when \ m_i < m_{yz} \leq m_j \qquad \tau = 1 - \left(\frac{m_{yz} - m_i}{m_j - m_i}\right)^{n_b} \qquad\qquad (17)$$

where the exponent n_b is a function of the m_y/m_z ratio and the n_z and n_y input values.

$$n_b = (n_z - n_y)e^{\left(\frac{-\pi}{5}\frac{m_y}{m_z}\right)} + n_y \qquad\qquad (18)$$

Eq. 18 is a nonlinear regression equation based on the assumption that n_b varies linearly with respect to ϕ from n_z to n_y ($0 \leq \phi \leq 90^o$). The angle ϕ given in Fig. 1 is simply a function of the m_y/m_z ratio where $\phi = tan^{-1}(m_y/m_z)$. The n_z and n_y values are exponents like that in Eq. 17 for the nonlinear stiffness reduction along the $\textbf{\textit{m}}_z$ and $\textbf{\textit{m}}_y$ axes in Fig. 1, respectively (Rosson and Ziemian 2019). The material model allows for the independent input of the n_z and n_y values, and the residual stress ratio c_r.

3. Inelastic Stiffness Matrix Terms

The stiffness reduction that occurs due to yielding over the member length is accounted for by using several beam elements per member and a stiffness matrix with coefficients that can vary depending on the severity of yielding at the initial and terminal nodes. Based on the assumption the tangent modulus varies linearly over the length of the element, the coefficient terms provide a

5

reasonable approximation of the reduced flexural and torsional stiffness of the element due to partial yielding. In practice, the error introduced by this assumption is reduced by using multiple elements along the length of the member. The stiffness matrix developed by Ziemian and McGuire (2002) was used in this study because the τ values from Eqs. 16 and 17 can be used directly as the a and b terms in Eqs. 19, 20 and 21. The stiffness matrix terms in Eqs. 19 and 20 are already in *MASTAN2*, but the stiffness terms in Eqn. 21 were developed and added to the source code.

In the following way, Eqs. 1 through 18 were used in a nonlinear material subroutine of *MASTAN2*. For a given W-shape, the dimensional properties were used to determine the constants λ, λ_0 and λ_1. Eqs. 1 and 2 were used to find m_{1z} and m_{1y} for a specified c_r condition. For a given m_z and m_y moment condition, the values m_{zi}, m_{yi} and m_i were determined using Eqs. 3 – 5. The m_z^* and m_y^* values were evaluated using Eqs. 6 and 7, and the C_1 and C_2 constants were found using Eqs. 9 and 10. With these two constants, and the given m_z and m_y condition, the m_{zj} value was found using Eq. 11 when $m_y/m_z \leq m_y^*/m_z^*$ and Eq. 12 when $m_y/m_z > m_y^*/m_z^*$. The m_{yj} and m_j values were found using m_{zj} in Eqs. 13 and 14, and m_{yz} was determined using Eq. 15. For a given m_z and m_y moment condition, the exponent n_b was found using Eq. 18 for specified n_z and n_y values. The stiffness reduction τ was found using Eq. 17 when $m_i < m_{yz} \leq m_j$; otherwise $\tau = 1$ when $m_{yz} \leq m_i$ from Eq. 16. The a term is the τ condition based on the m_z and m_y conditions at the initial node, and the b term is based on the m_z and m_y conditions at the terminal node. The terms in Eq. 21 can vary based on yielding due to St. Venant's torsion and the bimoment at the initial and terminal nodes. For this application of use it was decided to use the same a and b terms as those in Eqs. 19 and 20 because the stiffness reduction occurs primarily due to yielding of the cross-section from the bending moments m_z and m_y.

$$
\frac{EI_z}{L}
\begin{array}{cccc}
v_1 & \theta_{z1} & v_2 & \theta_{z2}
\end{array}
\begin{bmatrix}
\frac{12}{L^2}\left(\frac{a+b}{2}\right) & -\frac{6}{L}\left(\frac{2a+b}{3}\right) & -\frac{12}{L^2}\left(\frac{a+b}{2}\right) & -\frac{6}{L}\left(\frac{a+2b}{3}\right) \\
& 4\left(\frac{3a+b}{4}\right) & \frac{6}{L}\left(\frac{2a+b}{3}\right) & 2\left(\frac{a+b}{2}\right) \\
& & \frac{12}{L^2}\left(\frac{a+b}{2}\right) & \frac{6}{L}\left(\frac{a+2b}{3}\right) \\
\text{Sym.} & & & 4\left(\frac{a+3b}{4}\right)
\end{bmatrix}
\tag{19}
$$

$$
\frac{EI_y}{L}
\begin{array}{cccc}
w_1 & \theta_{y1} & w_2 & \theta_{y2}
\end{array}
\begin{bmatrix}
\frac{12}{L^2}\left(\frac{a+b}{2}\right) & -\frac{6}{L}\left(\frac{2a+b}{3}\right) & -\frac{12}{L^2}\left(\frac{a+b}{2}\right) & -\frac{6}{L}\left(\frac{a+2b}{3}\right) \\
& 4\left(\frac{3a+b}{4}\right) & \frac{6}{L}\left(\frac{2a+b}{3}\right) & 2\left(\frac{a+b}{2}\right) \\
& & \frac{12}{L^2}\left(\frac{a+b}{2}\right) & \frac{6}{L}\left(\frac{a+2b}{3}\right) \\
\text{Sym.} & & & 4\left(\frac{a+3b}{4}\right)
\end{bmatrix}
\tag{20}
$$

$$
\begin{array}{cccc}
\boldsymbol{\theta}_{x1} & \boldsymbol{\theta}_{x2} & \boldsymbol{\theta}'_{x1} & \boldsymbol{\theta}'_{x2}
\end{array}
$$

$$
GJ\begin{bmatrix}
\dfrac{6}{5L}\left(\dfrac{a+b}{2}\right) & -\dfrac{6}{5L}\left(\dfrac{a+b}{2}\right) & \dfrac{b}{10} & \dfrac{a}{10} \\[2mm]
 & \dfrac{6}{5L}\left(\dfrac{a+b}{2}\right) & -\dfrac{b}{10} & -\dfrac{a}{10} \\[2mm]
 & & L\left(\dfrac{3a+b}{30}\right) & -L\left(\dfrac{a+b}{60}\right) \\[2mm]
\textit{Sym.} & & & L\left(\dfrac{a+3b}{30}\right)
\end{bmatrix}
$$

$$
\begin{array}{cccc}
\boldsymbol{\theta}_{x1} & \boldsymbol{\theta}_{x2} & \boldsymbol{\theta}'_{x1} & \boldsymbol{\theta}'_{x2}
\end{array}
$$

$$
+\frac{EC_w}{L}\begin{bmatrix}
\dfrac{12}{L^2}\left(\dfrac{a+b}{2}\right) & -\dfrac{12}{L^2}\left(\dfrac{a+b}{2}\right) & \dfrac{6}{L}\left(\dfrac{2a+b}{3}\right) & \dfrac{6}{L}\left(\dfrac{a+2b}{3}\right) \\[2mm]
 & \dfrac{12}{L^2}\left(\dfrac{a+b}{2}\right) & -\dfrac{6}{L}\left(\dfrac{2a+b}{3}\right) & -\dfrac{6}{L}\left(\dfrac{a+2b}{3}\right) \\[2mm]
 & & 4\left(\dfrac{3a+b}{4}\right) & 2\left(\dfrac{a+b}{2}\right) \\[2mm]
\textit{Sym.} & & & 4\left(\dfrac{a+3b}{4}\right)
\end{bmatrix}
\tag{21}
$$

4. Material Model Validation Study

The validity of the new inelastic material model was verified by comparing its results with published finite element results by Subramanian and White (2017a, 2017b). Their finite element model used the full geometric and material nonlinear analysis capabilities of *ABAQUS*. The cross-section was modeled using S4 R shell elements with 20 elements through the web depth and 12 elements across the flange width. The element aspect ratio over the beam length was held to approximately 1.0 with the web elements. As part of their extensive study, W21x44 and W14x68 W-shapes were modeled with $C_b = 1$ and $C_b = 1.3$ end-moment conditions. To match their analysis conditions, the initial geometric imperfection was set to $L_b/2000$ at mid-span, bracing only at the supports, modulus of elasticity $E = 200\ GPa$ and yield strength $\sigma_y = 345\ MPa$. As given in Fig. 4, the *MASTAN2* model had 16 beam elements with continuous warping restraint over the entire length, except for the warping free conditions at both ends. The material model constants were $n_z = 1.5$, $n_y = 1.2$ and $c_r = 0.3$. The $\boldsymbol{M_z}$ moments in Fig. 4 were incrementally applied using a second-order inelastic analysis up to the limit load condition. In order to produce the $C_b = 1.3$ condition, the moment on the left end was modeled using $0.5\boldsymbol{M_z}$.
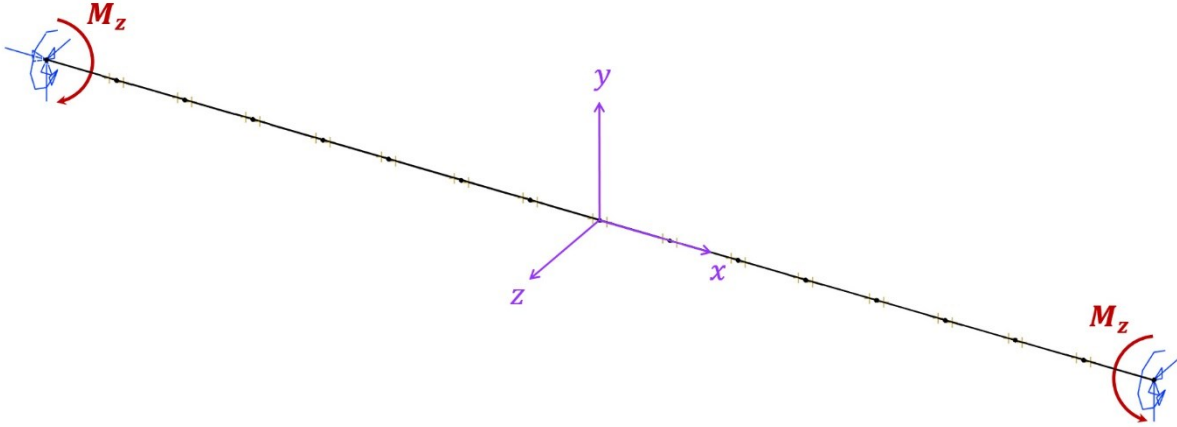
Figure 4: *MASTAN2* model of uniaxial bending condition with end moment M_z

The comparison results for the two W-shapes with $C_b = 1$ and $C_b = 1.3$ are given in Fig. 5. In general, the new model results agree very closely with the finite element results. The depth-to-flange-width ratio for the W21x44 ($d/b_f = 3.2$) and W14x68 ($d/b_f = 1.4$) are quite different, but despite this difference the accuracy of the new model seems to be unaffected by keeping the material constants the same for both W-shapes. A detailed discussion on why the finite element results are below the AISC curves can be found in the papers by Subramanian and White (2017a, 2017b). They proposed a reduced plateau length for L_p and a smaller maximum stress level for the elastic LTB limit. The new material model's results provide further substantiating evidence for these recommendations.

The new model was also verified by comparing results with the finite element results for the biaxial bending condition in Fig. 6 by Pi and Trahair (1994b). To match their analysis conditions, the 10UB29 steel I-section (*BHP* 1972) was modeled with an initial geometric imperfection of $L_b/1000$ at mid-span, bracing only at the supports, modified slenderness $\lambda = 1.029$, modulus of elasticity $E = 200\ GPa$ and yield strength $\sigma_y = 250\ MPa$. The *MASTAN2* model had 8 beam elements with continuous warping restraint over the entire length, except for the warping free conditions at both ends. The material model constants were the same as the previous verification study with $n_z = 1.5$, $n_y = 1.2$ and $c_r = 0.3$. Using a second-order inelastic analysis, the P_y load in Fig. 6 was incrementally applied first up to a specified magnitude, then the P_z load was incrementally applied up to the limit load condition. Maximum moments occur at the mid-span with components $M_z = P_y L/4$ and $M_y = P_z L/4$.

The finite element model used by Pi and Trahair (1994b) used a total Lagrangian nonlinear inelastic procedure with large deflection and large rotation capabilities. Their procedure assumed no local buckling or distortion, large deformations, material inelasticity, residual stresses, and initial crookedness and twist. Full details of the finite element model and method of solution are given in their companion paper (Pi and Trahair 1994a).
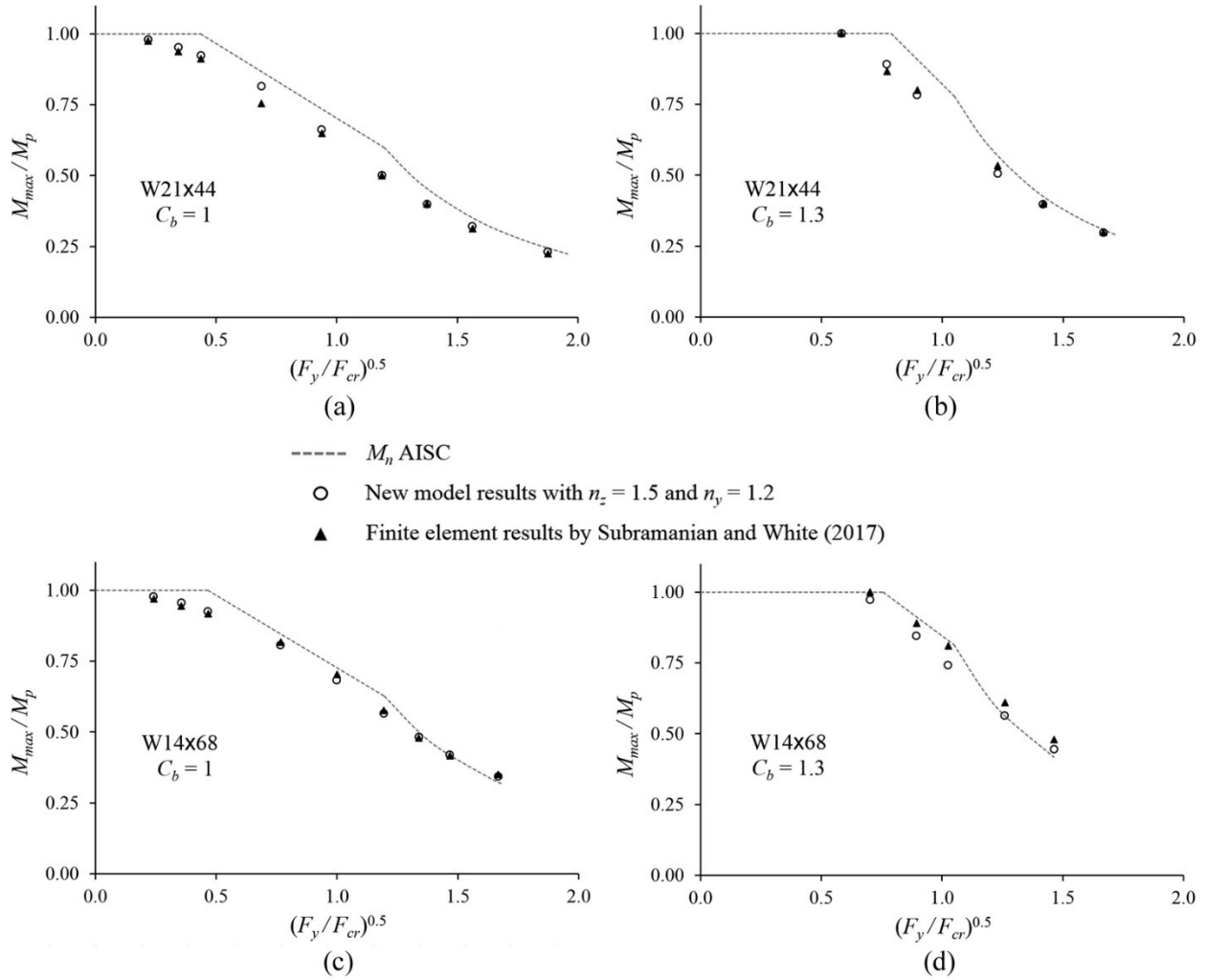
Figure 5: LTB comparison results for (a) W21x44 and $C_b = 1$; (b) W21x44 and $C_b = 1.3$; (c) W14x68 and $C_b = 1$; (d) W14x68 and $C_b = 1.3$
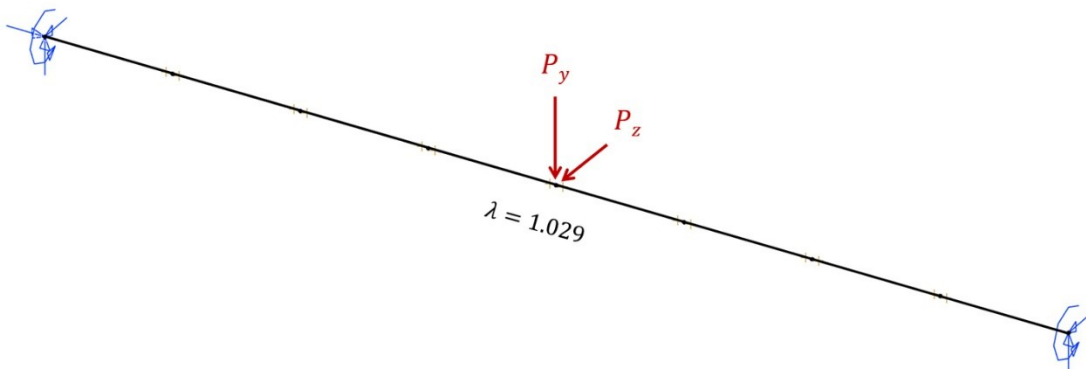

Figure 6: *MASTAN2* model of biaxial bending condition with mid-span loads P_y and P_z

9

The comparison results for the biaxial bending condition of the 10UB29 are given in Fig. 5. The new model results agree very closely with the finite element results by Pi and Trahair (1994b) using the same material constants as in the previous verification study.
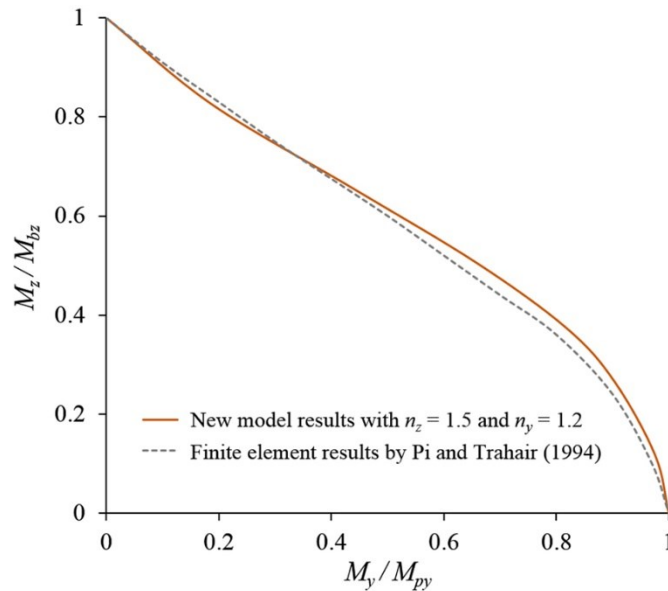

Figure 7: Biaxial bending comparison results for 10UB29

5. Uniaxial and Biaxial Beam Bending Study

Following the validation studies, analyses were conducted on simply supported beams using the new material model with uniaxial and biaxial bending end-moment conditions as given in Fig. 8. W-shapes with different depth-to-flange-width ratios were used to demonstrate the differences in the beam capacity results for the biaxial bending conditions when applying the same percentage of M_y/M_z moments. The analyses consisted of modeling a W21x93 ($d/b_f = 2.6$) and W12x72 ($d/b_f = 1.0$) with initial geometric imperfection of $L_b/2000$ at mid-span, bracing only at the supports, modulus of elasticity $E = 200\ GPa$ and yield strength $\sigma_y = 345\ MPa$. The *MASTAN2* model had 8 beam elements with the same warping restraint and material model constants as in the verification studies.
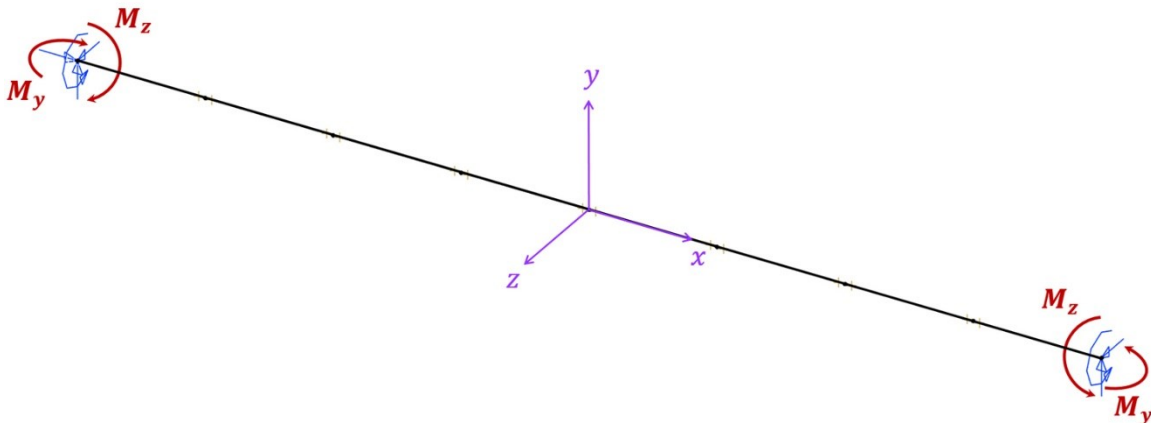

Figure 8: *MASTAN2* model of biaxial moment condition with end moments M_y and M_z

10

The biaxial bending conditions were modeled with both the M_z and M_y moments applied simultaneously and incrementally up to the limit load. The results in Fig. 9 indicate a significant difference in the biaxial bending moment responses for the two W-shapes. There is a much larger reduction in the capacity for the W21x93 compared with the W12x72 for the same percentage of M_y/M_z moments. As expected, the W12x72 with its smaller depth-to-flange-width ratio maintained higher biaxial bending capacities. The new material model also demonstrated its ability to provide consistent results over a range of M_y/M_z conditions.
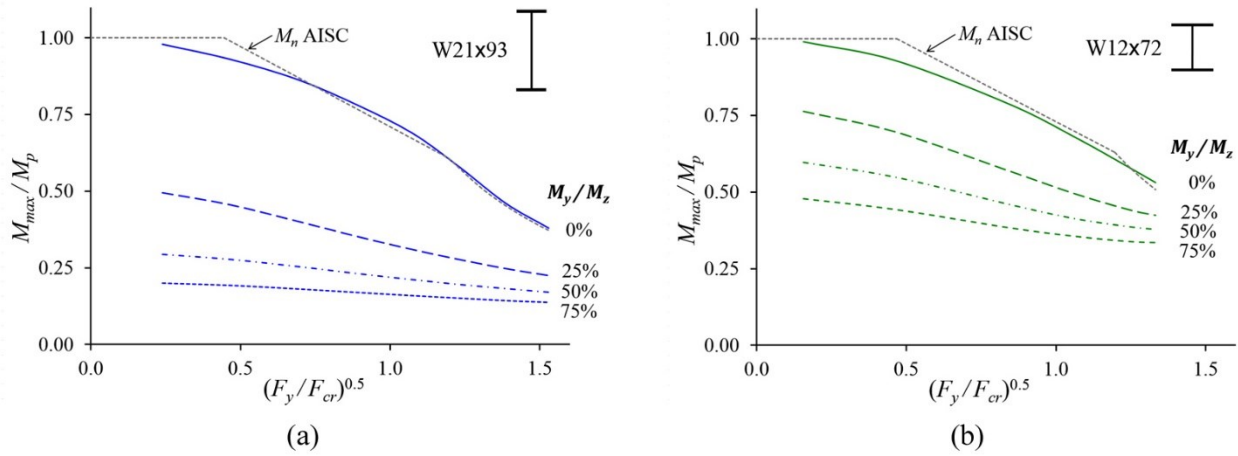

Figure 9: Uniaxial and biaxial bending results for (a) W21x93; (b) W12x72

6. Conclusions

A new inelastic material model for W-shapes under uniaxial and biaxial beam bending conditions is presented and validated. The material model was developed for use with a 14-DOF beam element in a second-order inelastic analysis. The model is based on the actual dimensions of a given W-shape and allows the user to specify the residual stress ratio c_r to control the initial yield condition and the exponent values n_z and n_y to control the rate of stiffness reduction. Validation studies compared the new model's results with those from detailed finite element analyses, and it was found that even when using the same material constants for all test conditions, the new model provided very comparable limit load results. The biaxial end-moment study using W-shapes with two different depth-to-flange-width ratios provided expected and consistent results over a range of moment conditions.

While the range of W-shapes and loading conditions were somewhat limited in this paper, the results indicate that the model can possibly be simplified by using a single exponent value since the two used in the study were so close to one another ($n_z = 1.5$ and $n_y = 1.2$). Further research is needed to verify this assumption and to study the new model for other W-shape dimensional properties, loading and bracing conditions, and warping end restraint conditions. Nonetheless, based on the results of this study, the new model can provide an accurate and effective means to account for the inelastic behavior of I-section beams with a 14-DOF beam element to satisfy the provisions of Appendix 1 in the AISC 360-16 *Specification for Structural Steel Buildings* (2016).

References

ABAQUS 6.12-1. Dassault Systèmes, Waltham, MA.

AISC. (2016). "Specification for structural steel buildings." *ANSI/AISC 360-16*, Chicago.

BHP hot rolled carbon steel sections and plates. (1972). Broken Hill Proprietary Co. Ltd., Melbourne, Australia.

ECCS (1984). "Ultimate limit state calculation of sway frames with rigid joints." *TC 8 of European Convention for Constructional Steelwork*, No. 33.

Kucukler M., Gardner L., Macaroni L. (2014). "A stiffness reduction method for the in-plane design of structural steel elements." *Engineering Structures*, 73 72-84.

MASTAN2, Version 3.5. Ziemian R.D., McGuire W.

Pi Y.L., Trahair N.S. (1994a). "Nonlinear inelastic analysis of steel beam-columns. I: Theory." *Journal of Structural Engineering*, 120(7) 2041-2061.

Pi Y.L., Trahair N.S. (1994b). "Nonlinear inelastic analysis of steel beam-columns. II: Applications." *Journal of Structural Engineering*, 120(7) 2062-2085.

Rosson B.T. (2016). "Elasto-plastic stress states and reduced flexural stiffness of steel beam-columns." *Proceedings of the 2016 SSRC Annual Stability Conference*, Orlando, Florida.

Rosson B.T., Ziemian R.D. (2019). "Validation study of a new inelastic material model for steel W-Shapes." *Proceedings of the 2019 SSRC Annual Stability Conference*, St. Louis, Missouri.

Subramanian L., White D.W. (2017a). "Reassessment of the lateral torsional buckling resistance of rolled I-section members: uniform-moment studies." *Journal of Structural Engineering*, 143 (4) 04016194.

Subramanian L., White D.W. (2017b). "Reassessment of the lateral torsional buckling resistance of rolled I-section members: moment gradient tests." *Journal of Structural Engineering*, 143 (4) 04016203.

Tankova T., Marques L., Andrade A., da Silva L.S. (2017). "A consistent methodology for the out-of-plane buckling resistance of prismatic steel beam-columns." *Journal of Constructional Steel Research*, 128 839-852.

Ziemian R.D., McGuire W. (2002). "Modified tangent modulus approach, a contribution to plastic hinge analysis." *Journal of Structural Engineering*, 128 (10) 1301-1307.